Building and Environment 228 (2023) 109838

Contents lists available at ScienceDirect

Building and Environment

journal homepage: www.elsevier.com/locate/buildenv

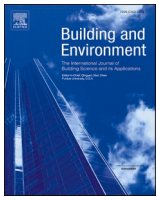

Simulation of moisture transport in fired-clay brick masonry structures accounting for interfacial phenomena

R. Ramirez [a,*], B. Ghiassi [b], P. Pineda [c], P.B. Lourenço [a]

[a] University of Minho, Department of. Civil Engineering, Campus de Azurém s/n, 4800-085, Guimarães, Portugal
[b] University of Birmingham, Department of Civil Engineering, School of Engineering, B15 2TT, Birmingham, United Kingdom
[c] Universidad de Sevilla, Department of Building Structures and Geotechnical Engineering, Avda. Reina Mercedes 2, 41012, Seville, Spain

ARTICLE INFO

Keywords:
Masonry
Moisture transport
Diffusivity model
Numerical simulation
Multi-layered material
Brick-mortar interface

ABSTRACT

This paper presents a numerical study on moisture transport in brick masonry walls with a special focus on the simulation of their hygric performance as well as the hydraulic phenomena at the brick-mortar interface. A diffusivity model based on Fick's law is used to describe the moisture transport accounting for both liquid and water vapor movement. The necessary hygric parameters are obtained directly from experimental tests or determined by curve fitting. The proposed model is validated with respect to water absorption and drying tests. The good-fitness of the results is qualitatively assessed and an overall good agreement is found between the simulated and measured curves. It is demonstrated that the chosen liquid water diffusivity expression needs to be adjusted to represent drying processes; the necessary adjustment is made through a diffusivity factor implemented in the original analytical expression. The interface impact on water absorption is introduced as a hydraulic resistance. Moreover, it is hypothesized that the presence of successive interfaces entails an additive in-series effect. Conversely, the interfacial impact on drying is negligible. Finally, the proposed model is extended to different modeling approaches commonly used for mechanical studies of masonry. The necessary input data, modeling methodology, advantages and disadvantages associated with each modeling strategy are also discussed. The present study points out the need of studying water absorption in multi-layered structures made up of constituents with relatively similar hygric behavior. In such cases, the impact of imperfect contact at the interface between materials is not negligible.

1. Introduction

Masonry is one of the most common building materials used in civil construction all around the world. Masonry facades make up a fundamental part of the building envelope and load-bearing walls work as an integral part of the structural system. It is known that the presence of moisture in masonry walls composed of bricks and mortar joints can strongly influence the behavior of the system, affecting the overall performance of the building: energy consumption [1,2], structural response [3–5], durability and service life [5,6].

Considering the impact of moisture-related processes on building performance, various models and numerical tools have been developed to simulate moisture transport in porous building materials, e.g. Refs. [7–9]. These models differ in their dimension (one-, two- or three-dimensional), the type of flow (steady-state, quasi-static or dynamic), the parameter used to describe moisture potential (moisture content, capillary pressure, relative humidity, or vapor pressure), the number of parameters needed as input information, etc. Most models for moisture transport have put their focus on homogenous porous materials, whereas the studies on multi-layered cases are still scarce. These multi-layered problems, however, are the most common scenario for building physics applications and demand specific requirements, such as the need to define a driving potential continuous across the interfaces, or the need for consideration of the interfacial impact on moisture transport.

The experimental studies focused on moisture transport in layered composites have been covered to some extent in the literature, e.g. Refs. [10–13]. Common findings from these works are the existence of interfacial phenomena, the mismatching properties between material layers, and the directionality or influence of stacking order. On the other

* Corresponding author. Institute for Sustainability and Innovation in Civil Engineering (ISISE), University of Minho, Campus de Azurém, s/n, 4800-058, Guimarães, Portugal.
E-mail address: id6955@alunos.uminho.pt (R. Ramirez).

https://doi.org/10.1016/j.buildenv.2022.109838
Received 28 June 2022; Received in revised form 7 November 2022; Accepted 19 November 2022
Available online 21 November 2022

hand, the experimental studies focused on moisture transport in masonry components and assemblies are still limited [14–16]. Likewise, only a few investigations have focused on interface modeling for mass transfer problems in masonry [17–21]. A unified approach to characterize the brick-mortar interfaces has not been reached yet. Moreover, the conclusions may vary from one author to another depending on the modeling technique and the eventual purpose of the simulation. For instance, as demonstrated by Vereecken et al. [19], modeling the whole masonry as a homogenous brick layer may be allowed to simulate certain scenarios. A similar approximation has been used by other authors for one-dimensional (1-D) hygrothermal simulations [22,23], whereas the most common approach for two-dimensional (2-D) analyses is the distinction of brick and mortar layers although any type of interfacial effect is usually neglected [23–25]. Nonetheless, several studies highlight the fact that moisture transport in masonry walls may be strongly affected by the interface resistance [17,21].

The impact of bed mortar joints and brick-mortar interfaces have been more extensively studied in the field of structural mechanics. Different computational strategies have been reported in the literature to deal with the mechanical analysis of masonry structures. Fig. 1 summarizes the most common approaches. In terms of complexity, there are two major types of modeling strategies, namely micro- and macro-modeling [26]. Several phenomenological models accounting for the microstructure of the material represent a further development within the micro-modeling approach [27]. The micro-modeling strategies account for the mechanical behavior of masonry by means of nonlinear interface elements, continuum elements with nonlinear behavior or a combination of both. In turn, macro-modeling strategies assume a homogenized continuum material usually described by nonlinear constitutive laws. Depending on the masonry texture or the level of complexity of the study, macro-models may assume isotropic or orthotropic continua.

Although the focus of these structural mechanics studies is usually different, several lessons may be learned from a cross-disciplinary approach. In this sense, certain parallelisms may be drawn between the mechanical and the moisture transport –eventually extensible to hygrothermal– modeling strategies. Moreover, couplings between the different fields may be created as well. For this type of multi-physics analyses, the link between the hygric and mechanical fields is usually established through a one-way simple coupling process. This implies that the moisture distribution is calculated first and the obtained hygric strains are used as initial input for the mechanical analysis by means of the total strain decomposition principle [28]. Furthermore, the influence of moisture content on certain mechanical properties may be considered as well [29].

In the present work, a moisture transport model is used to reproduce moisture-related phenomena in masonry materials. The main purpose is to capture both water absorption and drying processes in multi-layered composites such as masonry. First, the model is introduced together with the necessary assumptions and limitations. Subsequently, a succinct overview of the material properties and experimental methods is provided. Then, the numerical simulations are presented and the model is validated against the experimental results. It is demonstrated that the liquid water diffusivity function needs to be adjusted to represent drying processes; the necessary adjustment is made through a diffusivity factor implemented in the original analytical expression. Considering the multi-layered nature of the studied material, a special emphasis is placed on the presence of the interfaces and their impact on moisture flow. Interface hydraulic resistances are implemented to account for the imperfect interface contact between brick and mortar. The presence of successive interfaces requires increasingly higher resistance values, pointing out an additive in-series effect. Conversely, the impact of the interface resistances on drying cases is negligible. Finally, commonly used modeling strategies for mechanical studies of masonry walls are combined with the proposed moisture transport model. The necessary input data, modeling methodology, advantages and disadvantages associated with each modeling strategy are also discussed.

2. Moisture transport model

This section describes the multiphase model adopted for the simulations. The porous medium is made up of a matrix of interconnected pores inside a solid skeleton. This solid phase is assumed to be continuous, homogenous, inert (no chemical reactions), isotropic and non-deformable. On the other hand, pores are assumed cylindrical, with a homogenous, isotropic distribution inside the material. The void space defined by the pores is filled in different proportions with a liquid and a gaseous phase. The liquid phase is pure and incompressible, whereas the air phase is an ideal mixture of dry air and water vapor at atmospheric pressure. For simplicity, advective air flow is not implemented in the model and pressure gradients are considered negligible. Additionally, a local, instantaneous thermodynamic equilibrium is assumed between the liquid and gaseous phases. Based on this, the contributions of liquid water and water vapor may be combined to define a global moisture content. Nonetheless, the contribution of water vapor to the total moisture content is negligible. Knudsen flow is not considered, and it is assumed that the capillary forces are dominant so that the effect of gravity is neglected.

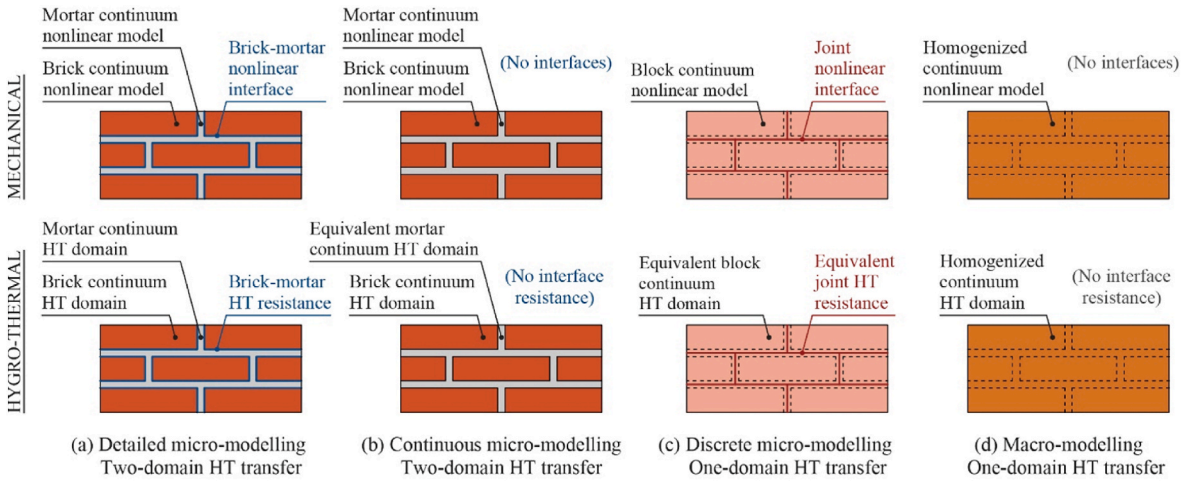

Fig. 1. Modeling strategies for masonry (adapted from Ref. [48], following [26,27]).

2.1. Governing equation

The chosen moisture transport model belongs to the so-called diffusivity approaches, which are based on Fick's laws of diffusion:

$$\frac{\partial w}{\partial \varphi}\frac{\partial \varphi}{\partial t} = \nabla \cdot \left(\frac{\partial w}{\partial \varphi} D_w \nabla \varphi\right) + \nabla \cdot \left(\frac{\delta_a}{\mu} \nabla (\varphi\, p_{v,sat})\right) \tag{1}$$

where w [kg/m^3] is the moisture content, φ [dimensionless] is the relative humidity, t [s] is the time, D_w [m^2/s] is the liquid water diffusivity, δ_a [kg/(m·s·Pa)] is the water vapor permeability of still air, μ [dimensionless] is the water vapor resistance of the material, $p_{v,sat}$ [Pa] is the saturation vapor pressure. In Eq. (1), the first term on the right-hand side represents liquid water transport, whereas the second term stands for water vapor diffusion. It must be noted that the moisture content is usually expressed either as mass of adsorbed water per volume of dry material, w [kg/m^3], or as mass of adsorbed water per mass of dry material, w_g [kg/kg], known as gravimetric moisture content. Both expressions are related through:

$$w = w_g \cdot \rho_{bulk} \tag{2}$$

where ρ_{bulk} [kg/m^3] is the bulk density of the porous material.

For the sake of simplicity, isothermal conditions are assumed, thus canceling additional thermal influences that could affect temperature-dependent parameters, such as relative humidity, water vapor permeability, etc.

Different analytical formulations may be found in the literature to account for the liquid water diffusivity. For the present study, a modified version of the exponential expression proposed by Künzel [30] is used:

$$D_w = \gamma \cdot \left(\frac{A_w}{w_{cap}}\right)^2 \cdot 10^{3 \cdot \left(\frac{w}{w_{cap}} - 1\right)} \tag{3}$$

where γ [dimensionless] is a diffusivity factor depending on the material and transport process (wetting/drying), A_w [kg/(m^2·s$^{0.5}$)] is the capillary absorption coefficient, and w_{cap} [kg/m^3] is the capillary moisture content. The original formulation by Künzel uses a fixed value of 3.80 for γ, which here is left as an adjustable parameter in order to accommodate a variety of materials a transport processes. The main advantage of the chosen expression comes from the fact that it is defined by means of reasonably simple measurable properties, such as the capillary absorption coefficient, plus it has only one adjustable parameter, which nonetheless guarantees a great deal of flexibility.

2.2. Interface modeling

The simulation of moisture transport in multi-layered materials –such as masonry– requires specific considerations due to the combination of media with different hygric properties and the presence of interfacial zones between consecutive layers [16–18,21]. In the context of the present studies, the interfacial zone between bricks and mortar is treated macroscopically, thus a phenomenological interface with zero thickness is assumed.

Considering the combination of dissimilar materials, due to the discontinuity between their moisture storage properties, a formulation based on a continuous potential, such as capillary pressure, vapor pressure, or –as the case here– relative humidity is necessary. Then, the type of interface contact must be considered. If the transition from one layer to the other has no impact on moisture transport, the interface is assumed to have perfect hydraulic contact. However, in most multi-layered materials, certain retardation of the moisture flux across the interface is observed, which reveals the existence of an imperfect hydraulic contact. This phenomenon can be attributed to the discontinuity between the pore structures of the materials (natural contact), the existence of an air gap between the adjacent layers, or a combination of both cases [17].

In order to account for these phenomena, Brocken [17] proposed the introduction of a parameter to describe the interface permeability, K_{IF} [s/m], or alternatively an interface resistance, R_{IF} [m/s]. It is noted that the interface –either perfect or imperfect contact– has zero thickness and no hygroscopic capacity. If a constant interface resistance is assumed, the water flow across the interface, g_{IF} [kg/(m^2·s)], can be described by:

$$g_{IF} = K_{IF}\frac{\partial p_c}{\partial x} = \frac{1}{1/K_{IF}}\frac{\partial p_c}{\partial x} = \frac{\Delta p_c}{\frac{1}{K_{IF}}\cdot\Delta x} = \frac{\Delta p_c}{R_{IF}} \tag{4}$$

where p_c [Pa] is the capillary pressure. Therefore, the imperfect hydraulic contact translates into a drop in capillary pressure across the interface. Since the presented model uses relative humidity as driving potential, a change of variable becomes necessary. Kelvin's law may be used to link relative humidity with capillary pressure:

$$p_c = \rho_w \cdot R_v \cdot T \cdot \ln \varphi \tag{5}$$

where ρ_w [kg/m^3] is the density of water, R_v [J/(kg·K)] is the universal gas constant for water vapor, and T [K] is the absolute temperature. Assuming the applicability of Kelvin's equation, the water flow across the interface can be redefined with respect to the relative humidity:

$$g_{IF} = K_{IF}\frac{\partial p_c}{\partial \varphi}\frac{\partial \varphi}{\partial x} = K_{IF}\frac{\rho_w \cdot R_v \cdot T}{\varphi}\frac{\partial \varphi}{\partial x} = \frac{\rho_w \cdot R_v \cdot T}{\varphi}\frac{\Delta \varphi}{\frac{1}{K_{IF}}\cdot\Delta x} = \frac{\rho_w \cdot R_v \cdot T}{\varphi}\frac{\Delta \varphi}{R_{IF}} \tag{6}$$

2.3. Initial and boundary conditions

The model is completed by introducing the initial and boundary conditions. In particular, the boundary conditions can be of Dirichlet (also called first) or Neumann (second) type. The Dirichlet boundary condition indicates:

$$\varphi = \overline{\varphi} \tag{7}$$

where $\overline{\varphi}$ [dimensionless] is the prescribed relative humidity at the boundary.

Conversely, the Neumann boundary condition is defined as a flux derived from a vapor pressure difference:

$$g = h_m \left(p_{v,ext} - p_v\right) \tag{8}$$

where g [kg/(m^2·s)] is the convective moisture flux, h_m [s/m] is the convective mass transfer coefficient, and $p_{v,ext}$ [Pa] and p_v [Pa] are the partial vapor pressures defined for the environment and at the model boundary, respectively. Partial vapor pressure and relative humidity are related by:

$$\varphi = \frac{p_v}{p_{v,sat}(T)} \tag{9}$$

where the saturation vapor pressure, $p_{v,sat}$ [Pa], may be described empirically as a non-linear function of temperature, T [K], such as [31]:

$$p_{v,sat} = 610.7[\text{Pa}] \cdot 10^{7.5 \cdot \left(\frac{T-273.15}{T-35.85}\right)} \tag{10}$$

3. Experimental results

A basic set of material properties and moisture transport parameters must be introduced as input for the model. Moreover, a series of experimental results are needed to derive additional properties via inverse analysis and to validate the simulation results. The following section provides a brief explanation of the studied materials together with the experimental procedures performed to obtain the necessary properties and validation data. The reader is referred to Ref. [14] for further details about the experimental methods and derived material parameters.

3.1. Materials and specimens

Due to the composite nature of masonry, experimental tests were performed at two levels: (a) constituent materials separately, and (b) multi-layered masonry specimens. The single materials selected for this study included extruded fired-clay brick (B), and a pre-mixed natural hydraulic lime (NHL) mortar, which was prepared in two formats, namely cast in molds (LM) and between bricks in masonry bed joints (LMJ). For the multi-layered specimens, a masonry wall was prepared using the same constituent materials. Then, masonry samples (B + LMJ) were extracted from the wall using a diamond coring wet drilling machine.

A schematic view of the tested specimens is presented in Fig. 2. Brick and mortar cubes were cut from whole brick units and molded mortar prisms, respectively. Additionally, lime mortar discs extracted from masonry bed joints were analyzed to determine differences with respect to the molded counterpart. The multi-layered specimens extracted from the masonry wall consisted of cylinders with different stacking arrangements, i.e. different B + LMJ configurations.

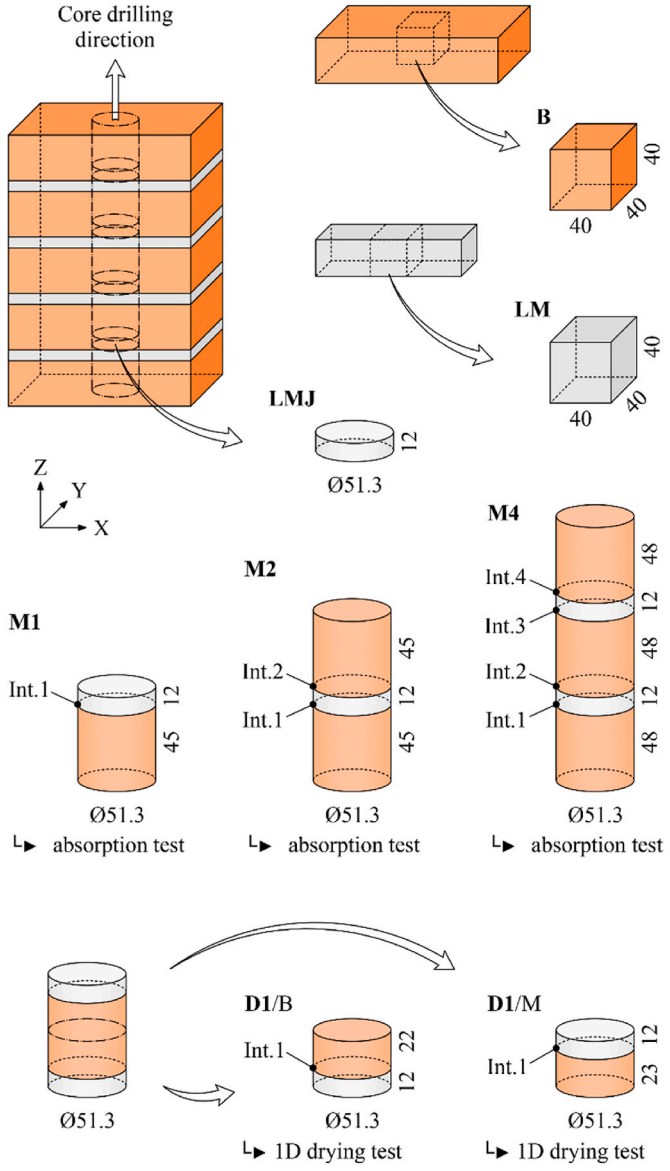

Fig. 2. Single-material and multi-layered specimens used for the experimental tests (schematic representation) (average dimensions in mm).

3.2. Methods

Five standardized tests were carried out to determine the generic and hygric properties of the studied materials. All the tests were conducted under controlled laboratory conditions.

Vacuum saturation tests were performed following the recommendations of RILEM TC [32]. An evacuation vessel was employed to remove the air from pre-dried specimens by application of vacuum. Then, water was introduced to saturate the samples. After a prescribed period, the specimens were weighed both under water (hydrostatic weight) and in the air. From the saturated mass measured in the air and under water, together with the dry mass, the open porosity, φ_o [dimensionless], bulk density, ρ_{bulk} [kg/m^3], and saturation moisture content, w_{sat} [kg/m^3], were calculated.

Capillary absorption tests were performed according to EN ISO 15148 [33] to determine the capillary absorption coefficient, A_w [kg/m^2/s$^{0.5}$], and the capillary moisture content, w_{cap} [kg/m^3]. For these tests, pre-dried specimens with sealed lateral faces were placed into a shallow water basin to ensure a 1-D capillary absorption. The water uptake mass plotted against the square root of time was used to define A_w as the slope of the first absorption stage. Additionally, the asymptotic value of the second stage was defined as w_{cap}.

Cup tests were used to measure the water vapor permeability, δ_v [kg/(m·s·Pa)], or alternatively the water vapor resistance, μ [dimensionless], by establishing different vapor pressures at both sides of the specimens. By determining the vapor flux across the material, the vapor permeability was calculated as described in ASTM E96/E96 M−10 [34], ISO 12572 [35], and EN 15803 [36].

Static gravimetric tests were performed according to ISO 12571 [37] to obtain the gravimetric equilibrium moisture content of the materials, w_g [kg/kg]. The specimens were exposed to a series of relative humidity conditions in a stepwise manner until equilibrium was reached. The discrete measurement points obtained from each step were then fitted into a moisture storage curve, also known as sorption isotherm, which characterizes the material capacity for moisture storage in the hygroscopic range.

One-dimensional drying tests were conducted as prescribed by EN 16322 [38], i.e. subjecting initially capillary saturated specimens to 1-D drying from a single surface. Drying tests do not provide direct material properties but are used to derive the moisture transport parameters by means of curve fitting, e.g. the liquid water diffusivity for drying.

3.3. Properties

The main material properties obtained from vacuum saturation, capillary absorption and cup tests are summarized in Table 1. Due to the extrusion manufacture, the studied bricks revealed a distinct anisotropic behavior and therefore three values are reported for the capillary absorption coefficient. Note that cup tests were only performed on bricks across the bed direction (Z). As expected, LM and LMJ showed distinct properties even though the mixes were prepared with the same composition and in the same controlled environment.

The data collected from static gravimetric tests are shown in Fig. 3. B and LM showed a low hygroscopic behavior and no hysteresis. Conversely, LMJ showed moisture adsorption for lower relative humidity values and a more marked hysteretic trend.

The static gravimetric measurements were fitted with common analytical expressions found in the literature. In particular, the model proposed by Künzel [30] was used to describe the sorption behavior of B and LM:

$$w(\varphi) = w_{cap} \cdot \frac{(\psi - 1)\cdot\varphi}{\psi - \varphi} \tag{11}$$

where $w(\varphi)$ [kg/m^3] is the moisture content as a function of relative humidity, w_{cap} [kg/m^3] is the capillary moisture content, and ψ

Table 1
Summary of material properties used for simulations.

Material	Property	Symbol	Value	Units	Source
B	Bulk density	ρ_{bulk}	1900	kg/m^3	Experimental
	Open porosity	φ_o	0.280	–	Experimental
	Capillary moisture content	w_{cap}	240	kg/m^3	Experimental
	Fitting parameter for sorption isotherm	ψ	1.0070	–	Experimental
	Water absorption coefficient (X-direction)	$A_{w,X}$	0.104	kg/(m^2·s$^{0.5}$)	Experimental
	Water absorption coefficient (Y-direction)	$A_{w,Y}$	0089	kg/(m^2·s$^{0.5}$)	Experimental
	Water absorption coefficient (Z-direction)	$A_{w,Z}$	0.061 [a]	kg/(m^2·s$^{0.5}$)	Experimental
	Water vapor resistance factor	μ	34.14	–	Experimental
LM	Bulk density	ρ_{bulk}	1990	kg/m^3	Experimental
	Open porosity	φ_o	0.255	–	Experimental
	Capillary moisture content	w_{cap}	225	kg/m^3	Experimental
	Fitting parameter for sorption isotherm	ψ	1.0066	–	Experimental
	Water absorption coefficient (isotropic)	$A_{w,ISO}$	0.235	kg/(m^2·s$^{0.5}$)	Experimental
	Water vapor resistance factor	μ	15.00	–	Ref. [49]
LMJ	Bulk density	ρ_{bulk}	2060	kg/m^3	Experimental
	Open porosity	φ_o	0.230	–	Experimental
	Capillary moisture content	w_{cap}	190	kg/m^3	Experimental
	Fitting parameter for adsorption isotherm	a_{ads}	4.26·10^{-6}	Pa^{-1}	Experimental
		m_{ads}	0.356	–	Experimental
	Fitting parameter for desorption isotherm	a_{des}	1.33·10^{-5}	Pa^{-1}	Experimental
		m_{des}	0.231	–	Experimental
	Water absorption coefficient (isotropic)	$A_{w,ISO}$	0.080	kg/(m^2·s$^{0.5}$)	Experimental
	Water vapor resistance factor	μ	15.00	–	Ref. [49]

[a] For multi-layered cases, $A_{w,B-Z} = 0.075$ kg/(m^2·s$^{0.5}$).

[dimensionless] is a fitting parameter. Künzel's model stems from a simplified form of the BET equation [39] and applies to sorption curves with a marked exponential trend. For B and LM, hysteresis was considered negligible, and the analytical curves were fitted using an average value of the absorption and the desorption processes, thus $\psi_B = 1.0070$ (Fig. 3a) and $\psi_{LM} = 1.0066$ (Fig. 3b).

On the other hand, the model proposed by Mualem [40] was used to describe the sorption behavior of LMJ. This model is a constrained form of the more generalized expression by van Genuchten [41]:

$$w(p_c) = w_{cap}\cdot\left[1 + (a\cdot p_c)^n\right]^{-m} \tag{12}$$

where $w(p_c)$ [kg/m^3] is the moisture content as a function of capillary pressure, p_c [Pa], and a [Pa^{-1}], n [dimensionless] and m [dimensionless] are fitting parameters. This model can better accommodate moisture storage curves with complex shapes and, therefore, is extensible to hygroscopic materials. In particular, Mualem's model establishes a correlation between the fitting parameters n and m, such as $m = 1 - 1/n$ [40], hence:

$$w(p_c) = w_{cap}\cdot\left[1 + (a\cdot p_c)^{1/(1-m)}\right]^{-m} \tag{13}$$

For LMJ, different trends were registered for adsorption and desorption. Thus, the hysteretic behavior was considered and two curves were defined: $a_{ads} = 4.26\cdot10^{-6}$ Pa^{-1} and $m_{ads} = 0.356$ for wetting, and $a_{des} = 1.33\cdot10^{-5}$ Pa^{-1} and $m_{des} = 0.231$ for drying (Fig. 3c).

4. Numerical simulations and discussion

The moisture transport model described in Section 2 is applied to simulate the hygric behavior of single materials (brick or mortar) and composite (masonry) specimens. Additionally, the material properties presented in Section 3 (Table 1) are used as numerical input parameters. For the multi-layered cases, the approach corresponding to the detailed micro-modeling strategy (Fig. 1a) is presented; the simulation of moisture transport considering other modeling approaches will be discussed in the following section. It must be noted that in this work, the accuracy of the model is considered based on the predictions of water uptake mass and moisture mass loss in capillary absorption and drying tests, respectively. Therefore, the global response of the system is used as a reference for validation. It is recalled, however, that a full validation would require the additional study of moisture profiles inside the specimens, which is out of the scope of the present paper.

All the simulations presented here are based on finite element analysis and were performed using COMSOL Multiphysics [42]. Since the analyzed cases can be reduced to 1-D phenomena, linear elements with quadratic shape functions were used for the discretization of the model. Preliminary sensitivity analyses were performed to determine the optimal mesh size and as a result, the average element size for all the models was set to 1 mm. The primary variable, i.e. φ, was interpolated based on standard Lagrangian shape functions. Moreover, backward finite difference method was used for automatic time discretization during the analysis. Finally, an iterative procedure based on the Newton–Raphson method was applied to solve the non-linear differential equations.

The imposed boundary conditions are summarized as follows:

a) Water absorption simulations; $\varphi = 1$ to represent liquid water at the base and $g = 0$ [kg/(m^2·s)] or null flux condition at the top face. The boundary condition at the base was introduced progressively using a smoothed step function.
b) Drying simulations; the bottom node was insulated whereas a convective flux was imposed at the top face, such as $g = h_m(p_{v,ext} - p_v)$, with $h_m = 6.05\cdot10^{-8}$ s/m. The partial vapor pressure of the environment was defined assuming $\vartheta = 23$ °C and $\varphi = 0.55$. Note that the value for the convective mass transfer coefficient was calculated from the drying tests performed on single materials as developed in Section 4.2.

Additionally, the initial conditions were taken as:

a) Water absorption simulations; $\varphi(t = 0) = 0$, i.e. dry conditions. For the multi-layered configurations, $\varphi = 0$ is incompatible with the definition of the moisture transfer coefficient applied at the interfaces (see Eq. (16)). Hence, for such cases a small value was assumed, i.e. $\varphi(t = 0) = 0.01$, which can still be considered equivalent to the dry state.
b) Drying simulations; $\varphi(t = 0) = 1$, i.e. capillary saturation.

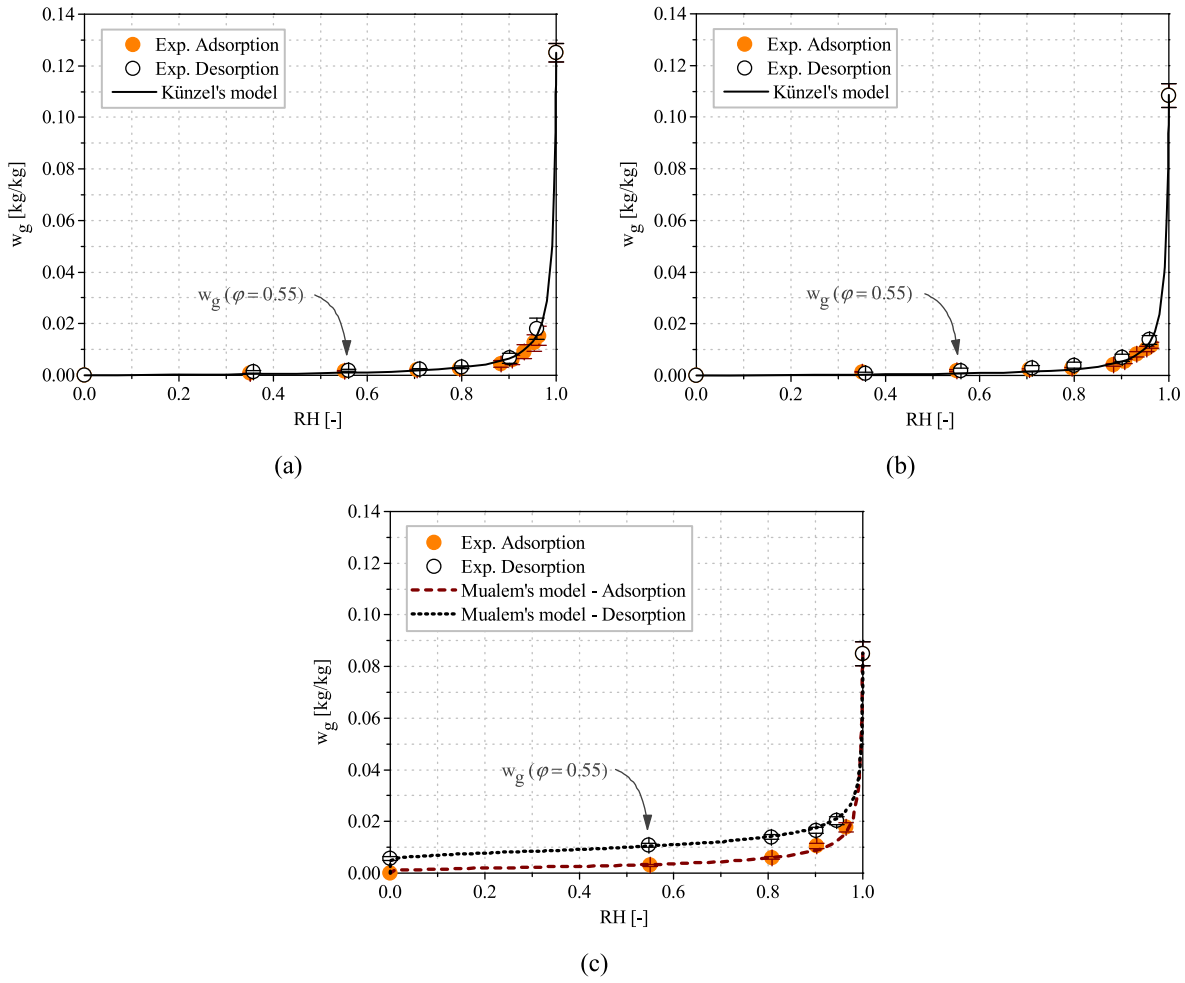

Fig. 3. Sorption isotherms and fitting curves for the studied materials at 23 °C: (a) B, and (b) LM, fitted with Künzel's model [30]; (c) LMJ fitted with Mualem's model [40].

Finally, a qualitative curve-fitting process was used to estimate the necessary hygric properties, namely the liquid water diffusivity for drying and the interface hydraulic resistance. Thus, the average trend of the measured data was used for comparison against the simulated curves to calibrate the corresponding parameters until an optimized solution was found.

4.1. Water absorption in single materials

The results for the capillary absorption tests on single materials, namely B and LM, are shown in Fig. 4 together with the simulated curves. From the comparison between experimental and numerical results, it is clear that the proposed moisture transport model can capture the observed behavior with great accuracy. For all the absorption cases, the diffusivity factor introduced in Eq. (3) was defined using the original value of γ proposed by Künzel [30], i.e. $\gamma_{ads} = 3.80$. The corresponding liquid diffusivity functions are shown in Fig. 5. Two other parameters were needed to determine the water uptake response of the model, namely (a) the capillary absorption coefficient, A_w, and (b) the capillary moisture content, w_{cap}. Note that both parameters were directly obtained from capillary absorption tests. As demonstrated by the numerical simulations, the capillary absorption coefficient is related to the water absorption rate: the higher A_w, the steeper the mass gain with respect to the square root of time. In other words, higher A_w values entail a faster absorption process, as expected. This relation is clearly evidenced by the studied materials since $A_{w,LM-ISO} > A_{w,B-X} > A_{w,B-Y} > A_{w,B-Z}$. On the other hand, w_{cap} determines the equilibrium plateau attained at the end of the absorption process, which can be verified from the volume of the specimen, V, such as $V[\mathrm{m}^3] \times w_{cap}[\mathrm{kg}/\mathrm{m}^3]$.

4.2. Drying in single materials

The results of the 1-D drying tests on single materials, namely B and LM, are shown in Fig. 6 together with the simulated curves. For these cases, an adjustment of the liquid water diffusivity function (Eq. (3)) was needed to match the experimental results. In particular, the diffusivity factor γ was indirectly estimated to calibrate the numerical response against the experimental data. The updated values of the diffusivity factor γ employed for drying cases, i.e. γ_{des}, are collected in Table 2. The corresponding liquid diffusivity functions are shown in Fig. 5.

The adjustment of the original liquid diffusivity function is in agreement with the studies by Scheffler [43], who discussed the existence of hysteretic transport functions for material models based on the diffusivity approach (Fick's law). Likewise, Krus [44] explained this phenomenon by the different velocities for wetting and drying processes. In other words, since drying and wetting occur at different rates, their corresponding liquid transport coefficients can differ. Therefore, two diffusivity functions are necessary, namely one for adsorption, $D_{w,ads}$, and one for desorption, $D_{w,des}$. However, no analytical expression is available in the literature specifically for drying. As an indication, Künzel [30] showed that for certain porous stones, the liquid diffusivity for desorption at capillary saturation could be approximately 3–5 times (finely porous stone) to one order of magnitude (coarse porous stone)

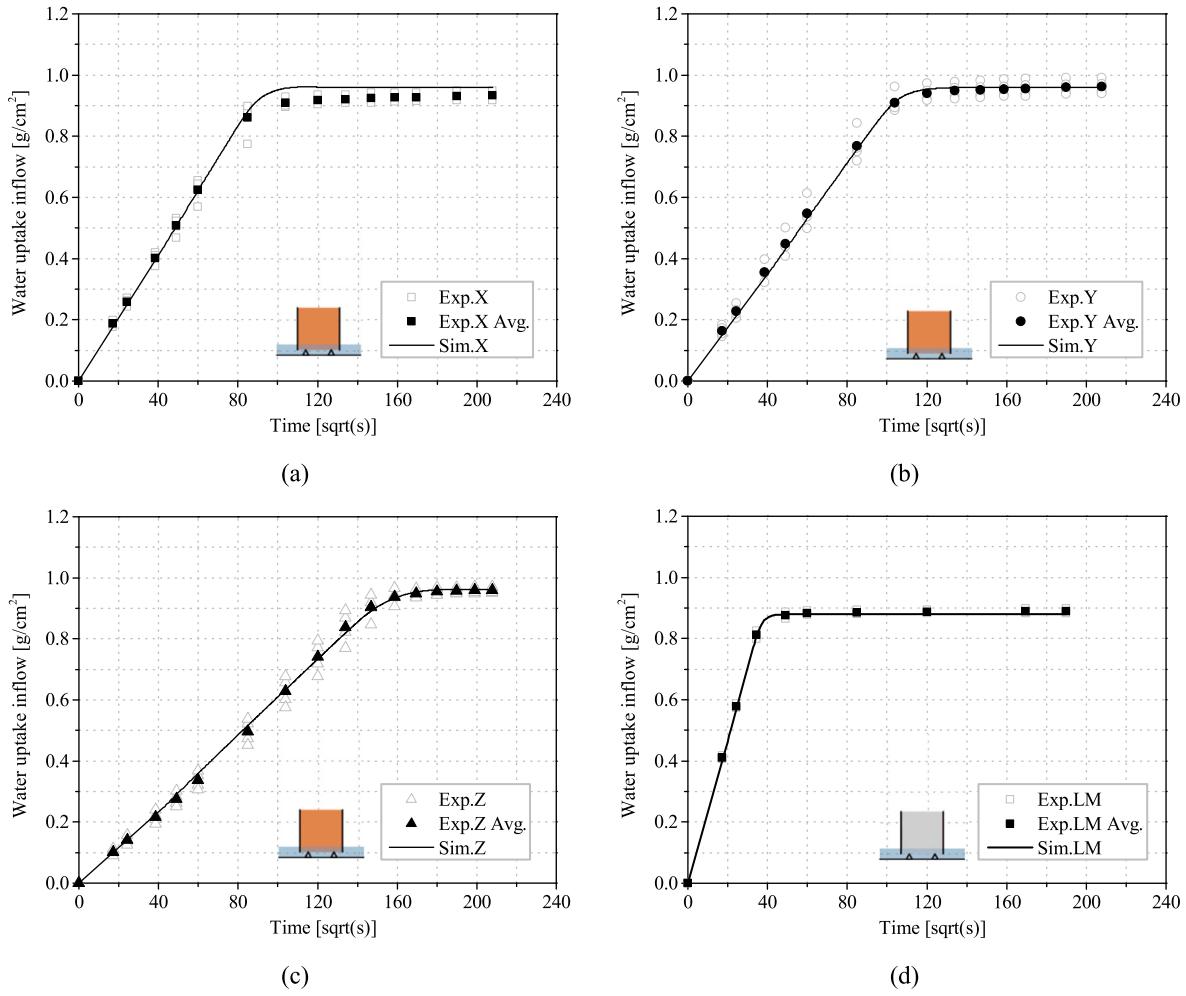

Fig. 4. Capillary absorption results for single materials: (a) B, X or extrusion direction; (b) B, Y or stretcher direction; (c) B, Z or bed direction; (d) LM, isotropic.

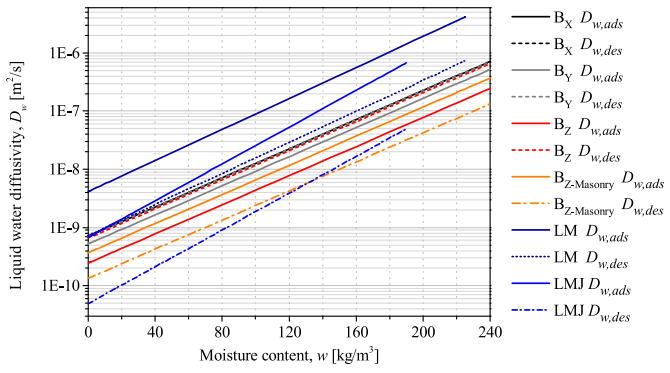

Fig. 5. Liquid water diffusivity functions employed in the simulations for the studied materials.

lower than the diffusivity for adsorption at w_{cap}. Other studies proved that the diffusivity for desorption can be adjusted by means of numerical simulations based on drying experiments [43]. For instance, Krus and Holm [45] proposed an analytical expression for the liquid water diffusivity as a function of moisture content. Their formulation can be directly applied to absorption cases, whereas for drying, a curve fitting process must be used to determine the diffusivity. For moisture conditions below 50% relative humidity, these authors proposed a fixed value $D_w = 2{\cdot}10^{-10}$ m^2/s, applicable to both transport processes. For higher moisture contents, however, drying would require a lower liquid transport coefficient. In particular, for their studied set of building porous materials, the relation $D_{w,abs}/D_{w,des}$ at capillary saturation ranged between 1.5 for fired-clay brick, 2.0–3.0 for natural stones and up to 5.0 for lime silica brick.

In the present study, the relation $D_{w,abs}/D_{w,des}$ at capillary saturation reached 5.67 for LM (Table 2), which is consistent with the literature and points out a significantly slower drying process compared to wetting. In fact, the drying simulation performed on LM using the adsorption diffusivity, i.e. $\gamma_{ads} = 3.80$, resulted into a much quicker mass loss with respect to the experimental evidence (see Fig. 6d). Interestingly, the behavior of the extruded fired-clay brick followed a different trend. The drying simulation for the extrusion direction, B_X, did not require any update to fit the experimental results, that is $\gamma_{des} = \gamma_{ads}$ (Fig. 6a). For the other two directions, however, the numerical results obtained using γ_{ads} resulted into lower mass loss rates when compared with the experimental data (Fig. 6b and c). Thus, $D_{w,abs}/D_{w,des} < 1$ for the stretcher and the bed directions of the brick, B_Y and B_Z, respectively. In other words, higher diffusivity values were needed to match the tests results. This behavior seems contrary to most trends described in the literature for porous building materials. However, a possible explanation can be found in the orthotropic nature of extruded bricks due to their manufacturing process. In fact, when analyzing the diffusivity values with respect to the extrusion direction, significant relations come to light (see Table 2). As concluded from the water absorption simulations, the orthotropic behavior of the studied brick is noticeable for adsorption, which is manifest in the relations $D_{w,ads,B-Y}/D_{w,ads,B-X} = 0.73$ and $D_{w,ads,B-Z}/D_{w,ads,B-X} = 0.34$ (values calculated at w_{cap}). Conversely, the

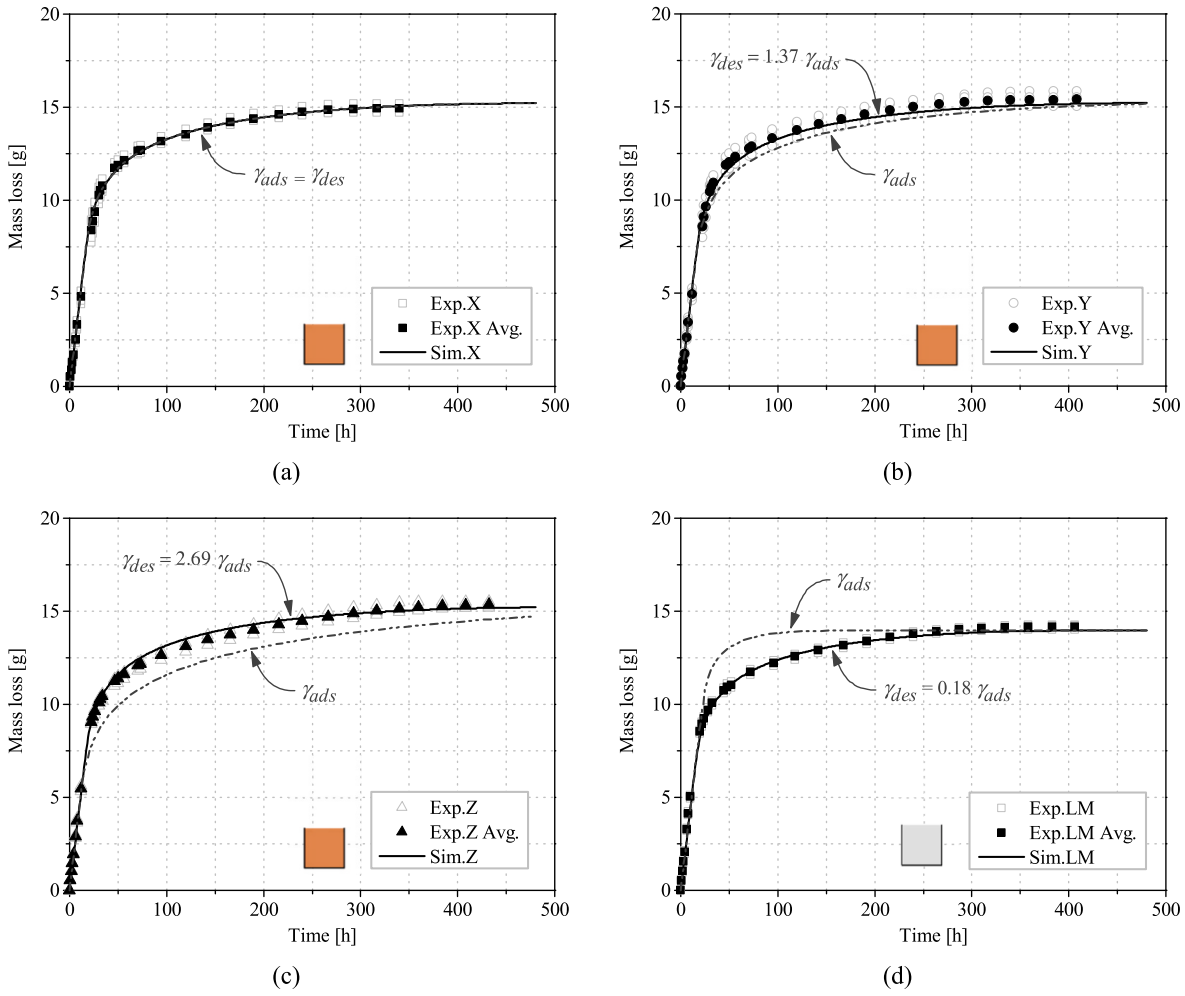

Fig. 6. Drying results for single materials: (a) B, X or extrusion direction; (b) B, Y or stretcher direction; (c) B, Z or bed direction; (d) LM, isotropic.

Table 2
Updated values of the diffusivity factor γ for drying.

Material/Direction	γ_{ads}	γ_{des}	$D_{w,ads}/D_{w,des}$ [a]	$D_{w,ads}/D_{w,ads,B-X}$ [a]	$D_{w,des}/D_{w,des,B-X}$ [a]
B_X	3.80	3.80	1.00	1.00	1.00
B_Y	3.80	5.19	0.73	0.73	1.00
B_Z	3.80 [b]	10.22 [b]	0.37	0.34	0.93
LM	3.80	0.67	5.67	–	–
LMJ	3.80	0.28	13.72	–	–

[a] Measured at capillary saturation, w_{cap}
[b] For multi-layered cases, $\gamma_{ads} = 3.80$; $\gamma_{des} = 1.37$.

diffusivity values for desorption show a more isotropic behavior, in particular $D_{w,des,B-Y}/D_{w,des,B-X} = 1.00$ and $D_{w,des,B-Z}/D_{w,des,B-X} = 0.93$ (values obtained at w_{cap}).

In the proposed moisture transport model, the parameter that controls the mass loss rate during the first drying stage (linear trend) is the convective mass transfer coefficient, h_m, which defines the convective flux imposed as boundary condition. Indeed, the value of the mass transfer coefficient was calculated from the linear mass loss phase assuming constant vapor flux and constant boundary conditions [43]:

$$h_m = \frac{j_v}{p_v(T_{surf}, \varphi_{surf}) - p_v(T_{env}, \varphi_{env})} \tag{14}$$

where j_v [kg/(m^2·s)] is the vapor mass flow density, and $p_v(T_{surf}, \varphi_{surf})$ [Pa] and $p_v(T_{env}, \varphi_{env})$ [Pa] are the vapor pressures defined at the exposed surface and for the environment, respectively. For this calculation, $\varphi_{surf} = 1$ was assumed at the material surface during the first drying phase. Moreover, the surface temperature, T_{surf}, was assumed as the wet bulb temperature corresponding to the conditions of drying air in the environment. In practice, h_m represents a phenomenological transfer parameter that summarizes thermo-dynamical and fluid-mechanical effects and is dependent on the environmental conditions, namely temperature, relative humidity and wind speed [12]. It must be noted that during the first drying stage, a temperature drop is expected at the exposed surface due to the evaporation of water [46]. In the moisture transport model, thermal variations are assumed to dissipate instantly so that the system is in constant thermal equilibrium with the environment. Nonetheless, if the temperature variations needed to be considered in detail, a coupled hygrothermal model could be employed

instead of the moisture transport model. In such circumstances, a convective heat flux boundary condition must be added to the exposed surface, such as:

$$q = h_T(T_{ext} - T) \tag{15}$$

where q [W/m^2] is the convective heat flux, h_T [W/(m^2·K)] is the convective heat transfer coefficient, and T_{ext} [K] and T [K] are the temperature of the environment and the model boundary, respectively. For hygrothermal simulations, the mass transfer coefficient is commonly linked to the heat transfer coefficient by means of the Lewis analogy, i.e. $h_{m,Le} = 7.7{\cdot}10^{-9}\ h_T$. As a reference for the cases presented in this work, the calibration of the convective transfer coefficients for hygrothermal simulations would lead to $h_T = 25$ W/(m^2·K) and $h_{m,Le} = 1.93{\cdot}10^{-7}$ s/m. Nonetheless, since the analysis of thermal processes was out of the scope

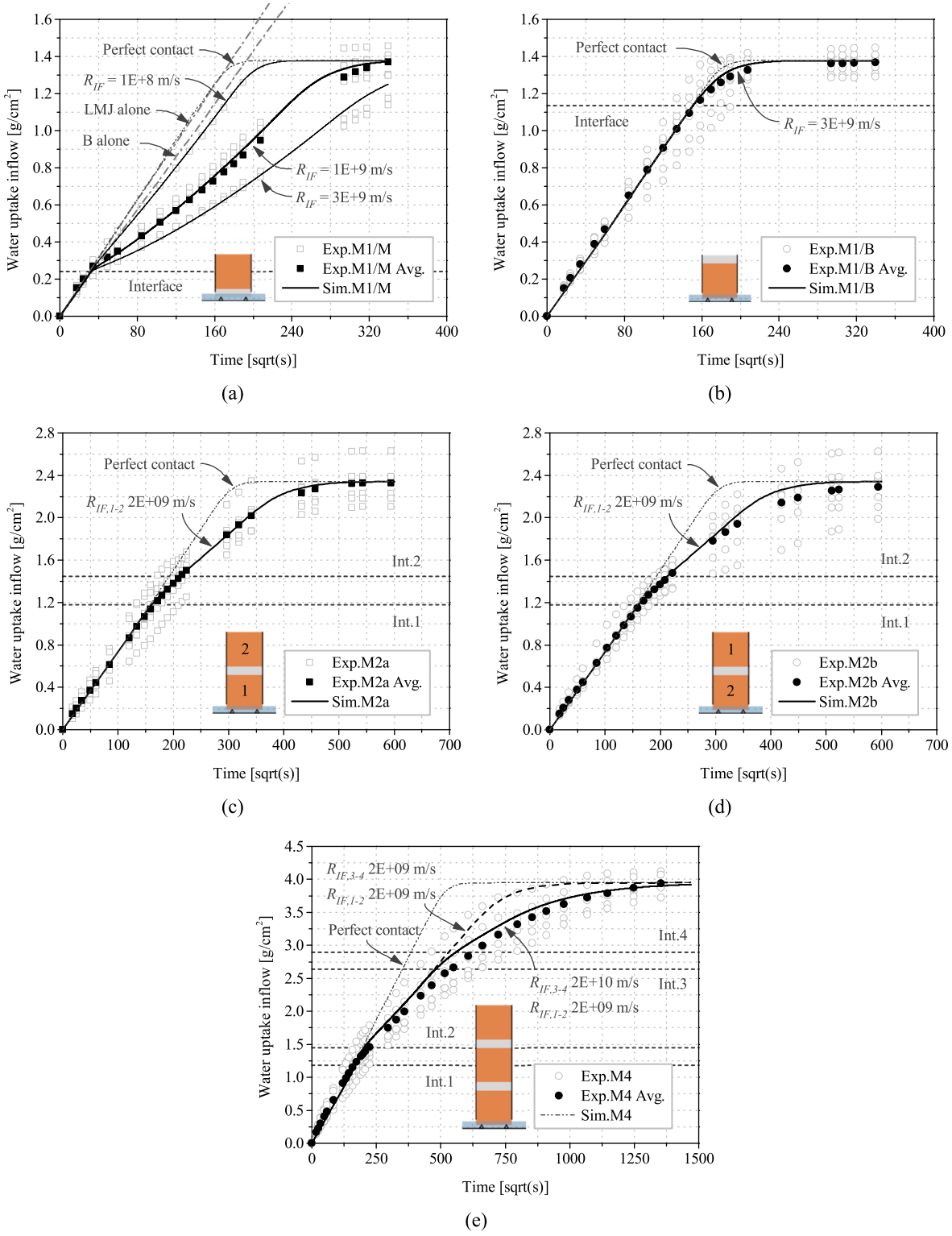

Fig. 7. Capillary absorption results for masonry specimens: (a) M1/M or LMJ-B configuration; (b) M1/B or B-LMJ configuration; (c) M2a or B1-LMJ-B2 configuration; (d) M2b or B2-LMJ-B1 configuration; (e) M4 or B-LMJ-B-LMJ-B configuration.

of this paper, the followed strategy focused on the moisture transport model and the mass transfer coefficient as the main variable for calibration. Notwithstanding this approximation, excellent trends were obtained for the first drying stage in all the studied cases.

On the other hand, the end of the first drying stage and the development of the second stage are dependent on the moisture transport properties, namely the liquid water diffusivity and to a lesser extent the water vapor permeability. The final state of equilibrium with the environment is defined for each material from the moisture storage function or sorption isotherm. In particular, the equilibrium moisture content corresponding to the prescribed drying environment, i.e. $\varphi = 0.55$, is individuated for the different cases in Fig. 3. Note that since the two studied materials (B and LM) are barely hygroscopic, their final moisture content is very close to dry conditions.

4.3. Water absorption in multi-layered materials

The results for water absorption on masonry specimens are presented in Fig. 7 together with the simulated curves. The location of the interfaces shown in the graphs is estimated from the volume of each material layer and the corresponding capillary moisture content, i.e. $\sum_i^n V_{bulk,i}$ [m^3] $\times$ $w_{cap,i}$ [kg/m^3].

It is noted that the existence of an interface resistance as presented in Eq. (6) was introduced in COMSOL as an internal boundary condition or barrier to the moisture flux:

$$\beta_{IF} = \frac{\rho_w \cdot R_v \cdot T}{\varphi \cdot R_{IF}} \tag{16}$$

where β_{IF} [kg/(m^2·s)] is the moisture transfer coefficient.

The first set of experimental tests involved masonry samples with two layers, namely B + LMJ, and therefore with a single interface. The same cylinders were analyzed twice, once absorbing water from the mortar side (Fig. 7a, configuration M1/M), and a second time absorbing water from the brick side (Fig. 7b, configuration M1/B). The presence of the interface was barely perceptible for the configuration M1/B. Conversely, a clear drop in the measured inflow rate was noticeable for the cylinders M1/M. Therefore, the existence of an imperfect hydraulic contact was confirmed by the change of inflow rate in M1/M samples. Moreover, the difference between M1/B and M1/M supports the assumption of a natural contact between brick and mortar, most surely derived from a discontinuity in their pore structure (smaller pores in LMJ). In other words, the impact of the interface depends on the direction of the moisture flux and is more pronounced when the transfer occurs from a finely porous material to a medium with coarser pores.

For the numerical simulations, the M1/M scenario was studied first (see Fig. 7a). A model assuming perfect contact (no hydraulic interface) showed mass gain rates within the range expected for the monolithic cases, that is considering the whole cylinder was brick or mortar. Then, the implementation of an interface resistance, R_{IF} as in Eq. (16), provided accurate results. To achieve the best fit, R_{IF} values were added iteratively. Three different cases were considered, as shown in Fig. 7a: (a) low impact interface, $R_{IF} = 0.1{\cdot}10^9$ m/s, with only a slight retardation of the water mass inflow; (b) middle impact interface, $R_{IF} = 1.0{\cdot}10^9$ m/s, corresponding to the average behavior of the experimental values; (c) higher impact interface, $R_{IF} = 3.0{\cdot}10^9$ m/s, which causes a more significant drop of the water absorption rate. Conversely, these three scenarios caused little variations of the results for the configuration M1/B, as shown in the Fig. 7b where the most severe case, $R_{IF} = 3.0{\cdot}10^9$ m/s, is depicted against the model assuming perfect contact. This phenomenon may be explained by the proximity of the interface to the top face of the specimen, which implies that the water front reaches the interface when the material is already close to its equilibrium state, i.e. capillary saturation. In such circumstances, any deviation in the moisture absorption rate caused by the interface is obscured by the transition of the mass uptake curve towards the final plateau.

The second group of analyses performed on masonry specimens consisted of cylinders with three layers, namely B + LMJ + B, thus two interfaces (Fig. 7c and d). Experimentally, the cylinders were tested twice, each time absorbing water from one of the opposite bricks, i.e. B1-LMJ-B2, labeled M2a configuration, and B2-LMJ-B1, labeled M2b configuration. For both situations, only a slight absorption retardation was perceived at the first interface, whereas a more noticeable drop was noticed when the water was moving from mortar to brick (second interface). Overall, the apparent equivalency between M2a and M2b cases reassured the assumption of a natural contact between the materials. In other words, the fact that the M2 specimens showed the same trend for both tested directions indicates that there are no localized defects at the interface and most surely the cause of the imperfect hydraulic contact is the discontinuity between the pore structure of the adjacent materials. Numerically, accurate results were obtained when an interface resistance $R_{IF} = 2.0{\cdot}10^9$ m/s was applied at the two interfaces.

Finally, water absorption analyses were performed on masonry specimens with five layers, B + LMJ + B + LMJ + B, thus four interfaces (M4). The experimental results and the simulated mass gain curves are presented in Fig. 7e. The trends observed for the previous cases are applicable to M4 cases as well, in particular the lesser impact of the brick-to-mortar interface. It is noted that when the same hydraulic resistance applied for M2 cases was used, i.e. $R_{IF,1} = R_{IF,2} = R_{IF,3} = R_{IF,4} = 2.0{\cdot}10^9$ m/s, the simulation provided an acceptable response for the first two interfaces but it failed to capture the mass gain drop caused by the second mortar layer. Considering the experimental evidence and the simulation results, it is hypothesized that the successive appearance of interfaces gives rise to an additive retardation effect over the moisture flux. Consequently, a much higher resistance value was required for the second pair of interfaces to match the experimental data. In particular, a good fit was obtained when two sets of interface resistances were used, namely $R_{IF,1} = R_{IF,2} = 2.0{\cdot}10^9$ m/s for the first two interfaces (to be consistent with the previously studied configuration, M2), and $R_{IF,3} = R_{IF,4} = 2.0{\cdot}10^{10}$ m/s for the third and fourth interfaces.

4.4. Drying in multi-layered materials

The results of drying tests and simulations on masonry specimens are presented in Fig. 8. Two configurations were studied, namely cylinders drying from the brick face, labeled D1/B, and cylinders drying from the mortar face, D1/M. The convective mass transfer coefficient used for drying simulations in single materials, i.e. $h_m = 6.05{\cdot}10^{-8}$ s/m, was employed for multi-layered cases as well. Overall, the match with the average behavior of the experimental data is evident.

As it was mentioned for the drying studies on single materials, updating the diffusivity factor γ was necessary to calibrate the numerical response of multi-layered drying cases as well. In particular, the calibration process consisted of a parallel iterative tuning of $\gamma_{des,B}$ and $\gamma_{des,LMJ}$, so that the model could fit both experimental scenarios. Overall, it was found that the diffusivity of the material exposed to the environment was the most decisive parameter for each case. In other words, D1/B was more sensitive to variations in $\gamma_{des,B}$, whereas D1/M was mostly defined by $\gamma_{des,LMJ}$. As a result of the updating process, the corresponding values for the diffusivity factors were found, namely $\gamma_{des,B} = 1.37$ and $\gamma_{des,LMJ} = 0.28$ (Table 2). The diffusivity factor for LMJ showed the same trend defined in Section 4.2 for the molded mortar, LM, in this case with an even greater difference between adsorption and desorption ($D_{w,abs}/D_{w,des} = 13.72$ at w_{cap}).

For the brick material in multi-layered specimens, however, the updated liquid diffusivity followed a different trend compared to the drying cases of single-brick cubes. On this occasion, the factor γ_{des} needed to be reduced with respect to the wetting diffusivity in order to accommodate a slower mass loss rate ($D_{w,abs}/D_{w,des} = 2.77$ at w_{cap}). It must be noted that, despite deviating from the observations made for

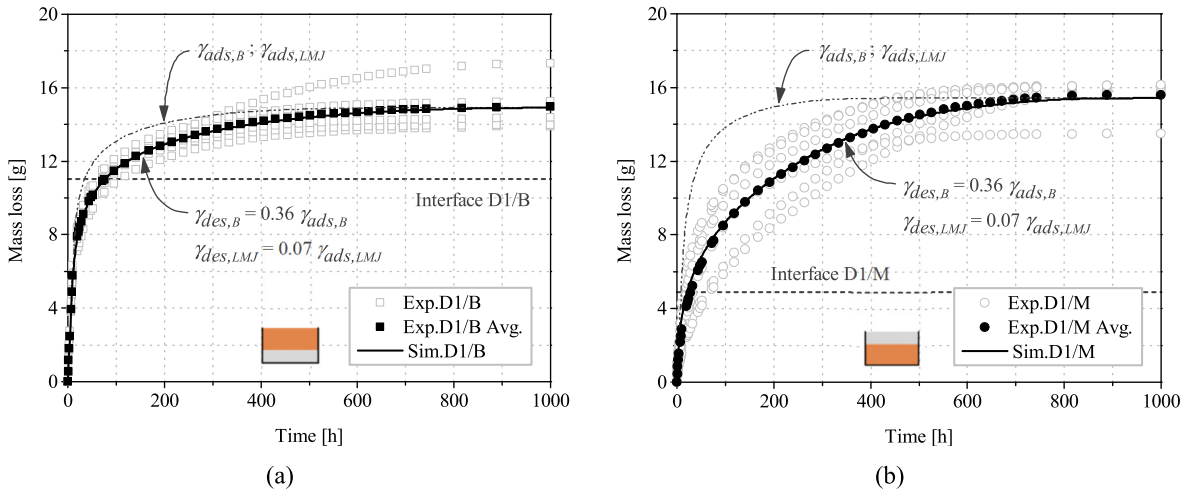

Fig. 8. Drying results for masonry specimens: (a) D1/B or drying-from-brick configuration; (b) D1/M or drying-from-mortar configuration.

mono-layered brick cases, this behavior is in line with the studied mortars and other materials reported in the literature [30,45]. Nonetheless, considering that the bricks used in masonry specimens showed a different capillary absorption coefficient (Table 1), variability of the material could be at the base of these dissimilarities as well.

The possible impact of the interfaces was also studied as part of the drying response of multi-layered specimens. Simulations assuming both perfect and imperfect contact were performed. However, by considering R_{IF} values as the ones proposed for the absorption cases, the results obtained with and without the interface resistance were virtually the same. The imposed R_{IF} needed to be in the order of $2.0{\cdot}10^{10}$ m/s (the highest value used in the absorption simulation M4) in order to produce a slight deviation with respect to the perfect contact case. Therefore, it was acknowledged that the presence of natural contact interfaces plays a minor role in the drying process of multi-layered masonry specimens. This fact supports the conclusions of the experimental studies in Ref. [14], in which the authors could not identify any interfacial effect on drying kinetics. In view of this, the perfect contact assumption can be applied to drying cases studied individually. For analyses involving both absorption and drying, the interface resistance must be tuned with respect to the wetting phase; it can be equally applied to the desorption process as it will not alter the response. For instance, the simulated curves reported in Fig. 8 were obtained with an interface resistance $R_{IF} = 1.0{\cdot}10^{9}$ m/s, as the middle impact interface defined for the absorption case M1/M.

5. Application to masonry models

In the previous section, an application of the detailed micro-modeling approach (Fig. 1a), was presented and validated for water absorption and drying processes. The current section describes the extension of the moisture transport simulations to other modeling strategies commonly used for mechanical studies of masonry. The same experimental data presented previously were used here as well. In particular, the water absorption tests performed on masonry specimens M2 and M4 were employed as case studies. Thus, the corresponding moisture transport analyses were performed assuming the other strategies presented in Fig. 1, namely continuous micro-modeling approach (Fig. 1b), discrete micro-modeling approach (Fig. 1c), and macro-modeling approach (Fig. 1d). Additionally, a comparison between the different strategies is presented in terms of accuracy, level of complexity, flexibility, requirements, and limitations.

In general, an iterative curve-fitting procedure was used to calibrate the numerical parameters and obtain a good correlation between simulated and experimental results. In particular, the models with explicit account for the interfaces (detailed micro- and discrete micro-) were calibrated by tuning the interface resistance R_{IF} whereas the models without interfaces (continuous micro- and macro-) were calculated using the diffusivity factor γ as fitting parameter.

Moreover, an averaging procedure was used to calculate the equivalent properties needed for the discrete micro- and the macro-modeling approaches, which rely on homogenization. This concept is based on the volume fraction of each material with respect to the total volume, in the original configuration. Therefore, an equivalent property X_{EQ} is calculated as:

$$X_{EQ} = \sum_{i}^{n} X_i \frac{V_i}{V_{Total}} \tag{17}$$

where X represents the original value of the studied parameter, V is the volume, and i represents the material layer in a n-layered composite.

It must be noted that the constituent materials, B and LMJ, have been defined in the present work by two different moisture storage models (Fig. 3). In the current section, the distinction between the sorption isotherms was kept for the models with explicit consideration of the two materials (detailed micro- and continuous micro-). However, for the models with an equivalent continuum (discrete micro- and macro-), a simplification was employed, and the sorption isotherm of the brick alone (Künzel's model) was chosen to be representative of the equivalent behavior. It is noted that this generalization is applicable to capillary-active materials and absorption processes, in which the porous medium is exposed to high relative humidity boundary conditions. In such circumstances, mass transport is governed mainly by liquid water movement [47]. In other words, the absorption process involves the uppermost portion of the moisture storage curve. However, the same generalization might prove faulty in drying simulations with hygroscopic materials, such as LMJ. For such cases, the equivalent behavior could be captured more accurately through a Mualem's type formulation (see Eq. (13)).

5.1. Continuous micro-modeling

The moisture transport equation and boundary conditions presented in Section 2 were applied to simulate the water absorption in M2 and M4 specimens by means of a continuous micro-modeling strategy (Fig. 1b). For the continuous micro-modeling approach, brick and mortar were modeled with their original properties, that is as obtained experimentally or with the corresponding values taken from the literature (Table 1). In order to account for the interfacial impact on moisture flux, the diffusivity factor γ associated to the mortar joints was tuned until a good agreement with the experimental data was found. Hence, the

necessary parameters and updated material properties are presented in Table 3 and the corresponding results are shown in Fig. 9a and b.

Note that when the original $\gamma_{ads,LMJ} = 3.80$ is used, the problem is equivalent to the detailed micro-model with perfect contact (no interface resistance). The best match is found when the diffusivity factor is reduced to a 10 % of its original value, that is $0.10 \times \gamma_{ads,LMJ}$. Additionally, for the M4 configuration, different γ values were needed to account for the incremental effect of successive interfaces. The best fit was obtained with $0.10 \times \gamma_{ads,LMJ}$ for the first interface (to be consistent with the previous case) and $0.02 \times \gamma_{ads,LMJ}$.

In terms of requirements, the same input material parameters demanded by the detailed micro-modeling approach are needed for the continuous micro-model. The latter does not implement hydraulic interfaces and therefore the calibration must be done through the diffusivity factor γ. Since there are no interfaces, the complexity of the model is relatively lower. In general, the continuous micro-modeling approach can provide good accuracy of results and it may be recommended in cases where interfaces need to be explicitly avoided.

5.2. Discrete micro-modeling

The results for water absorption simulations using the discrete micro-modeling strategy (Fig. 1c) are presented in Fig. 9c and d. The necessary parameters and updated material properties are presented in Table 3. Considering the discrete micro-modeling strategy, masonry was represented by the combination of two components: the bricks were modeled as a continuum with equivalent material properties and extended size, whereas interfaces were used to simulate the presence of mortar joints and brick-mortar interfaces. If the properties of both materials are known, the volume fraction of each material may be used to define equivalent properties. Otherwise, brick properties may be assumed without compromising the accuracy (see curves using brick *versus* equivalent brick properties in Fig. 9c and d).

The main parameter used for calibration within the discrete micro-model strategy are the hydraulic resistances, R_{IF}, imposed at the interfaces. It was found that a value $R_{IF} = 4.0{\cdot}10^9$ m/s provided a good fit for the M2 configuration. Note that this value is double the resistance originally used for the detailed micro-model. This is expected since now a single interface must stand for the two interfaces of the detailed micro-model. On the other hand, two sets of values were used to match the experimental results of M4 configuration, namely $R_{IF} = 4.0{\cdot}10^9$ m/s for

Table 3
Input parameters used for the masonry modeling strategies (highlighted cells show calibration parameters).

Modeling strategy	Case study	Material / Element	Parameters							
			γ_{ads} [-]	w_{cap} [kg/m^3]	ψ [-]	a [Pa^{-1}]	m [-]	A_w [a] [kg/(m$^2{\cdot}$s$^{0.5}$)]	μ [-]	R_{IF} [m/s]
Detailed micro-	M2	B	3.80	240	1.0070	-	-	0.075	34.14	-
		LMJ	3.80	190	-	4.26E-6	0.356	0.080	15.00	-
		Int.1 / 2	-	-	-	-	-	-	-	2.0E+9
	M4	B	3.80	240	1.0070	-	-	0.075	34.14	-
		LMJ	3.80	190	-	4.26E-6	0.356	0.080	15.00	-
		Int.1 / 2	-	-	-	-	-	-	-	2.0E+9
		Int.3 / 4	-	-	-	-	-	-	-	2.0E+10
Continuous micro-	M2	B	3.80	240	1.0070	-	-	0.075	34.14	-
		LMJ*	0.40	190	-	4.26E-6	0.356	0.080	15.00	-
	M4	B	3.80	240	1.0070	-	-	0.075	34.14	-
		LMJ1*	0.40	190	-	4.26E-6	0.356	0.080	15.00	-
		LMJ2*	0.08	190	-	4.26E-6	0.356	0.080	15.00	-
Discrete micro-	M2	Eq.B	3.80	234	1.0070	-	-	0.076	31.84	-
		Int.1	-	-	-	-	-	-	-	4.0E+9
	M4	Eq.B	3.80	232	1.0070	-	-	0.076	31.21	-
		Int.1	-	-	-	-	-	-	-	4.0E+9
		Int.2	-	-	-	-	-	-	-	4.0E+10
Macro-	M2	Eq.B	3.04	234	1.0070	-	-	0.076	31.84	-
	M4	Eq.B	3.04	232	1.0070	-	-	0.076	31.21	-

[a] For 2-D models, B and Eq.B have orthotropic behavior, $A_{w,x} = 0.104$ kg/(m$^2{\cdot}$s$^{0.5}$).

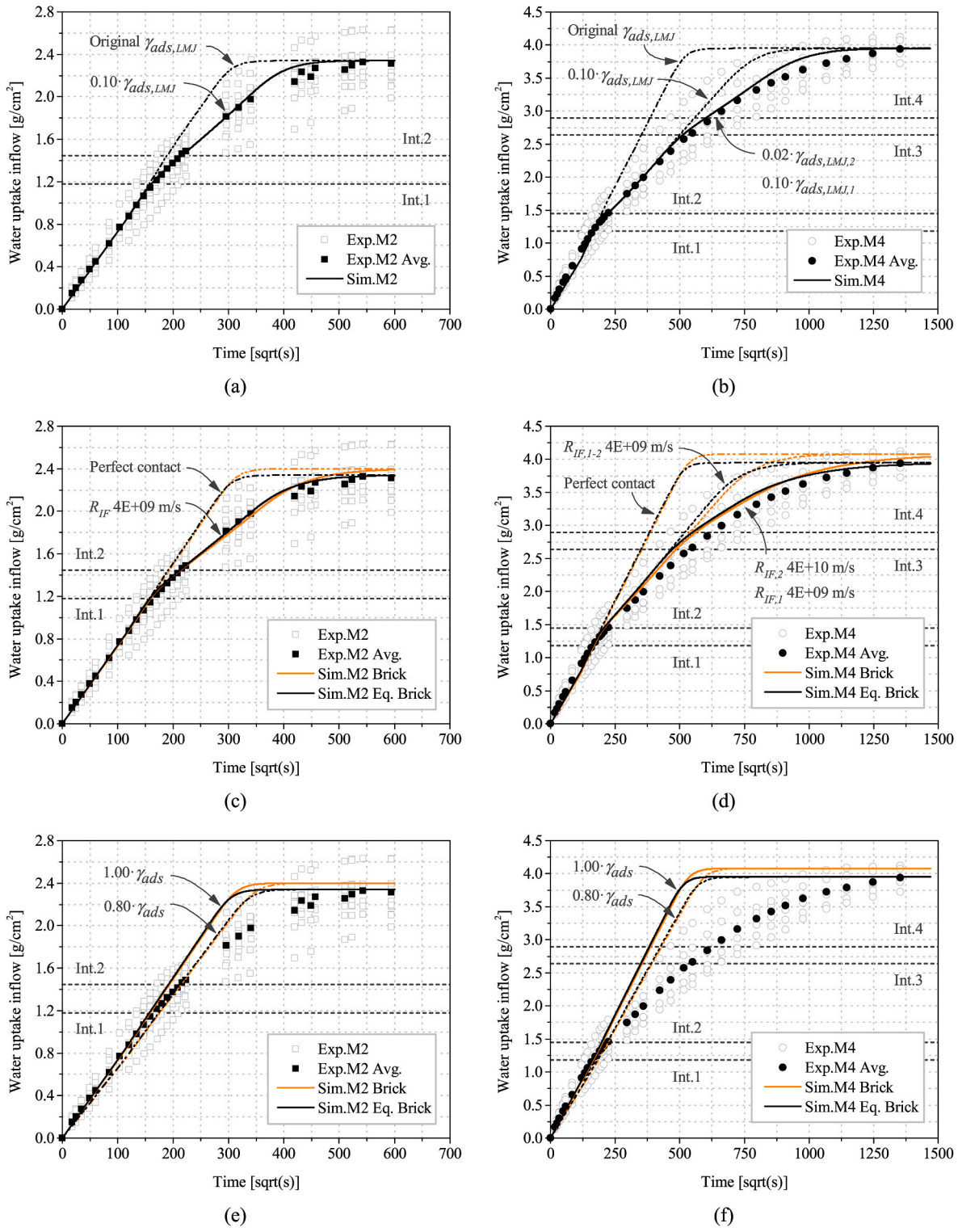

Fig. 9. Water absorption simulated using different modeling strategies: (a) Continuous micro-modeling, M2; (b) Continuous micro-modeling M4; (c) Discrete micro-modeling, M2; (d) Discrete micro-modeling M4 (e) Macro-modeling, M2; (f) Macro-modeling, M4.

the first interface (consistent with the M2 case) and $R_{IF} = 4.0{\cdot}10^{10}$ m/s for the second interface. The higher value for the second interface is consistent with the hypothesis of an in-series interfacial phenomenon, that is the additive effect of successive interfaces. Once again, it is noted that the value imposed at the second interface is double the resistance used for the corresponding detailed micro-modeling case.

In terms of requirements, the discrete micro-modeling approach has the advantage of needing fewer input material parameters than the other micro-modeling approaches. If the properties of brick and mortar are known, an equivalent material may be calculated by volume averaging as presented in Eq. (17). Otherwise, the model may produce considerably accurate results assuming only the properties of the brick (contrast curves produced using brick *versus* equivalent brick properties in Fig. 9c and d). This simplification is valid as long as the volume proportion of

masonry units is higher than the corresponding volume of mortar joints, which is usually the case in brickwork masonry. Due to the extended geometry of the bricks, the geometric definition of the system may be somewhat more complex than the other strategies. On the other hand, the model is simplified by assuming only one material. Moreover, interfaces can capture localized phenomena such as the imperfect contact between adjacent layers.

Overall, the discrete micro-modeling technique provides high accuracy and is a good compromise between simplicity and quality of results. Its use is encouraged when mortar properties are not known.

5.3. Macro-modeling

Finally, water absorption simulations were performed considering a macro-modeling strategy (Fig. 1d). The results are shown in Fig. 9e and f. Following the macro-modeling approach, masonry was idealized as a continuum with equivalent material properties. On this occasion, the homogenized medium must capture the overall behavior of the system so that it provides an average trend. As in the discrete micro-modeling case, the volume fraction of each material may be used to define equivalent properties if both brick and mortar parameters are known. Otherwise, brick properties may be applied to the system and similar results can be obtained (see curves using brick *versus* equivalent brick properties in Fig. 9e and f).

The diffusivity factor γ was used as a calibration parameter for curve-fitting. The curves obtained with the original factor $\gamma_{ads} =$ 3.80 were able to capture the initial water uptake but largely overestimated the absorption rate as time evolved. This was expected since it is the usual response of a monolithic specimen (see absorption of single materials in Fig. 4). For the M2 configuration, a reduction of the diffusivity parameter, e.g. 0.80 $\times$ γ_{ads}, was needed to produce a water uptake curve that could fit the overall experimental envelope. This type of correction provides an average approximation: the initial absorption rate is underestimated, whereas the absorption rate for prolonged times is overestimated. Note that the same reduction applied to M4 cases is not quite satisfactory since it deviates considerably from the experimental results.

Macro-modeling approaches are commonly used for global structural analyses and their application to moisture transport is conveniently straightforward. The geometry is very simple and only one material is modeled. Moreover, the properties of brick and mortar may be used to define an equivalent medium or solely brick properties may be considered. Nonetheless, this strategy proves very little flexibility, and the simulation cannot capture the changes in moisture flux with evolving time or localized phenomena such as the existence of hydraulic interfaces. Overall, the accuracy of the macro-model approach is far lower than the one achievable via micro-modeling.

5.4. Rising damp in a masonry wallette

To further demonstrate the capabilities of the proposed approach, a two-dimensional (2-D) masonry wallette was studied under capillary absorption conditions. This type of analysis is representative of rising damp, which is a rather common phenomenon in load-bearing masonry structures. The wallette was modeled using the different strategies previously explained, namely detailed micro-, continuous micro-, discrete micro- and macro-modeling. The geometry of the wallette is that presented in Fig. 1 for each modeling technique, assuming symmetry conditions through the middle vertical plane. In the original configuration, the bricks had dimensions 200 mm $\times$ 100 mm $\times$ 50 mm and the mortar joints were 12 mm thick. The same brick and mortar materials previously presented for the multi-layered masonry cases and the different modeling approaches were used here (Table 3). Additionally, the orthotropic response of bricks was considered in the 2-D simulations and the capillary absorption coefficient for the extrusion direction was used for brick and equivalent brick materials, i.e. $A_{w,X} =$ 0.104 kg/(m^2·s$^{0.5}$) (Table 1).

The finite element mesh used for all the models consisted of quadrilateral Lagrangian quadratic elements with average size 2 mm. The total amount of elements for each model was around 11,000. To represent rising damp exposure, the boundary conditions were taken as for free water absorption, namely direct contact with water at the base, $\varphi = 1$, and null flux, $g = 0$ kg/(m^2·s), at the top face. The boundary condition at the base was introduced progressively using a smoothed step function. Sealed conditions were assumed for the lateral faces and symmetry was imposed at the mid-section vertical plane. Finally, 'dry' initial conditions were considered, $\varphi(t = 0) = 0.01$.

The results obtained with the different modeling strategies are presented in Fig. 10 in terms of evolution of the internal relative humidity with time. For the models with an explicit account of the mortar joints (detailed micro-, Fig. 10a, and continuous micro-modeling, Fig. 10b), the presence of vertical joints became relevant. This was expected since the studied NHL mortar, either molded (LM) or cast directly in masonry bed joints (LMJ), showed a higher capillary absorption coefficient than brick. Higher A_w entails a higher liquid water diffusivity and consequently the joints in masonry act as a moisture bridge, accelerating the absorption. In the present simulations, this fact was particularly evident in the vertical joints, in which the moisture front advanced faster than in the adjacent bricks. Note that this phenomenon is in contrast with other cases with cement mortar, where the less permeable cement acts as a moisture barrier [21].

Only slight differences in moisture distribution were registered for the detailed micro- (Fig. 10a) and the continuous micro-modeling approaches (Fig. 10b). The discrete micro-model (Fig. 10c) could not capture the disturbances induced by the vertical joints but overall, the obtained moisture front evolution was quite accurate. Finally, the macro-modeling strategy (the presented results were calculated with a correction 0.80 $\times$ γ_{ads}) revealed the same flaws anticipated in Section 5.3 for this type of approach, namely underestimation of the initial moisture absorption and overestimation of the absorption rate for prolonged times. A common feature presented by all the models was a continuous diffusion of the moisture front with evolving time. In other words, the wet front –normally assumed sharp– became dimmer and dimmer as it advanced through the material.

6. Conclusions

This paper presents a moisture transport model to study a series of moisture-related phenomena in multi-layered porous materials, namely water absorption and drying. First, experimental tests are described together with the necessary input parameters and validation data. Then, numerical simulations based on the finite element method are performed with the aid of COMSOL Multiphysics. Experimental and simulated results are compared, and material parameters are calibrated to improve curve fitting.

A set of generic and hygric-related material properties are needed as input for the model: bulk density, open porosity, capillary moisture content, capillary absorption coefficient, moisture storage curves (adsorption/desorption), and water vapor permeability/resistance. Moreover, two parameters are chosen as calibration variables to fit the experimental results. In particular, the interface hydraulic resistance is chosen as the calibration parameter for water absorption tests, whereas the diffusivity factor γ defined for the liquid water diffusivity function is used to calibrate drying.

The expression for liquid water diffusivity (Eq. (3), originally proposed by Künzel [30]) is validated with water absorption and drying tests results. However, it is demonstrated that the diffusivity function needs to be adjusted depending on the process (wetting/drying). A diffusivity factor γ is proposed as an adjustable parameter to accommodate both processes. The original analytical formulation with $\gamma_{ads} =$ 3.80 can be used directly for the wetting processes together with the water absorption coefficient calculated from capillary absorption tests.

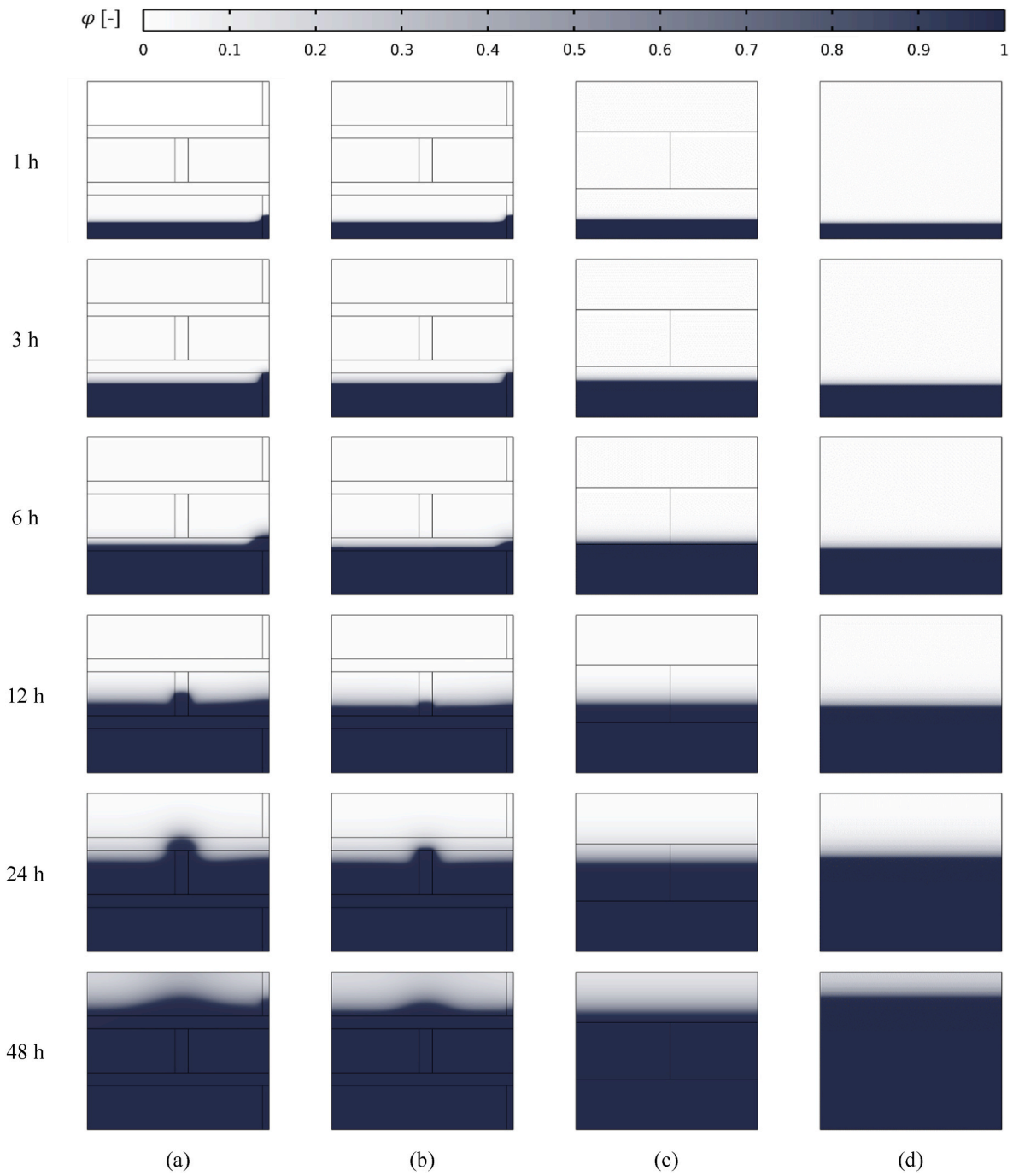

Fig. 10. Evolution of internal relative humidity in masonry wallettes simulated using different modeling strategies: (a) Detailed micro-modeling; (b) Continuous micro-modeling; (c) Discrete micro-modeling; (d) Macro-modeling.

Conversely, the expression for diffusivity in desorption processes lacks a consistent definition, thus inverse analysis from experimental data is needed for each case.

No analytical approach was found to evaluate the interface hydraulic resistance consistently. The interface behavior depends on the materials in contact, the geometric arrangement of the layers and specific conditions of each case, such as the existence or not of previous discontinuities. In the current work, the interface impact was estimated for water absorption cases by an iterative process of curve-fitting. The implemented interface resistances had a negligible impact on drying kinetics. Considering the case-specific issues derived from the interfacial contact, direct extrapolations of the presented resistance values must be treated with caution. Further works are needed to define a general approach for the study of moisture-related interface phenomena.

Different modeling approaches commonly used in solid mechanics for masonry structures and materials are extrapolated to the study of moisture transport problems. Considering the higher accuracy and flexibility of the models with an explicit account of interfaces, the use of the detailed micro- or the discrete micro-modeling techniques is encouraged. All the analyzed moisture transport modeling strategies are suitable for coupling with mechanical studies to define hygro-mechanical models.

Overall, the proposed moisture transport model is able to capture water absorption and drying processes in multi-layered masonry materials with considerable accuracy. Further works should extend the studies to non-isothermal problems, incorporating the necessary

temperature-dependent properties. Likewise, the application of transient boundary conditions (cyclic temperature and relative humidity) is a necessary step forward to reproduce service-life applications. Finally, subsequent studies should account for the presence of vertical joints and possible moisture bridges through open cracks.

Funding

This work was financed by national funds through FCT - Foundation for Science and Technology, under grant agreement SFRH/BD/117114/2016 attributed to the first author.

CRediT authorship contribution statement

R. Ramirez: Writing – original draft, Visualization, Validation, Software, Methodology, Investigation, Formal analysis, Conceptualization. **B. Ghiassi:** Writing – review & editing, Supervision, Methodology, Conceptualization. **P. Pineda:** Writing – review & editing, Supervision, Methodology, Conceptualization. **P.B. Lourenço:** Writing – review & editing, Supervision, Methodology, Funding acquisition, Conceptualization.

Declaration of competing interest

The authors declare that they have no known competing financial interests or personal relationships that could have appeared to influence the work reported in this paper.

Data availability

Data will be made available on request.

References

[1] M. Harrestrup, S. Svendsen, Full-scale test of an old heritage multi-storey building undergoing energy retrofitting with focus on internal insulation and moisture, Build. Environ. 85 (2015) 123–133, https://doi.org/10.1016/j.buildenv.2014.12.005.
[2] E. Vereecken, L. van Gelder, H. Janssen, S. Roels, Interior insulation for wall retrofitting – a probabilistic analysis of energy savings and hygrothermal risks, Energy Build. 89 (2015) 231–244, https://doi.org/10.1016/j.enbuild.2014.12.031.
[3] D.v. Bompa, A.Y. Elghazouli, Compressive behaviour of fired-clay brick and lime mortar masonry components in dry and wet conditions, Mater. Struct. 53 (2020) 60, https://doi.org/10.1617/s11527-020-01493-w.
[4] A.M. D'Altri, S. de Miranda, Environmentally-induced loss of performance in FRP strengthening systems bonded to full-scale masonry structures, Construct. Build. Mater. 249 (2020), 118757, https://doi.org/10.1016/j.conbuildmat.2020.118757.
[5] B. Ghiassi, P.B. Lourenço (Eds.), Long-term Performance and Durability of Masonry Structures: Degradation Mechanisms, Health Monitoring and Service Life Design, first ed., Woodhead Publishing, 2019 https://doi.org/10.1016/C2016-0-03710-5.
[6] X. Zhou, D. Derome, J. Carmeliet, Analysis of moisture risk in internally insulated masonry walls, Build. Environ. 212 (2022), 108734, https://doi.org/10.1016/j.buildenv.2021.108734.
[7] J.F. Straube, E.F.P. Burnett, Overview of hygrothermal (HAM) analysis methods, in: H.R. Trechsel (Ed.), Moisture Analysis and Condensation Control in Building Envelopes – ASTM Manual Series MNL 40, American Society for Testing and Materials, Philadelphia, 2001, pp. 81–89.
[8] H. Hens, Modeling the heat, air, and moisture response of building envelopes: what material properties are needed, how trustful are the predictions? J. ASTM Int. (JAI) 4 (2007) 1–11, https://doi.org/10.1520/JAI100460.
[9] H.M. Künzel, A.N. Karagiozis, A.H. Holm, A hygrothermal design tool for architects and engineers (WUFI ORNL/IBD), in: H.R. Trechsel (Ed.), Moisture Analysis and Condensation Control in Building Envelopes – ASTM Manual Series MNL 40, American Society for Testing and Materials, Philadelphia, 2001, pp. 136–151.
[10] M.A. Wilson, W.D. Hoff, C. Hall, Water movement in porous building materials—XIII. Absorption into a two-layer composite, Build. Environ. 30 (1995) 209–219.
[11] M.A. Wilson, W.D. Hoff, C. Hall, Water movement in porous building materials—XIV. Absorption into a two-layer composite (SA < SB), Build. Environ. 30 (1995) 221–227.
[12] C. Hall, W.D. Hoff, Water Transport in Brick, Stone and Concrete, second ed., CRC Press, London, 2009.
[13] E. Vereecken, P. Schůtová, S. Roels, How effective is kaolin clay for the creation of a perfect hydraulic interface contact between materials?, in: E3S Web of Conferences., vol. 172, 2020, 14002, https://doi.org/10.1051/e3sconf/202017214002.
[14] R. Ramirez, B. Ghiassi, P. Pineda, P.B. Lourenço, Experimental characterization of moisture transport in brick masonry with natural hydraulic lime mortar, Build. Environ. 205 (2021), 108256, https://doi.org/10.1016/j.buildenv.2021.108256.
[15] C. Groot, J. Gunneweg, The influence of materials characteristics and workmanship on rain penetration in historic fired clay brick masonry, Heron 55 (2010) 141–154.
[16] H. Janssen, H. Derluyn, J. Carmeliet, Moisture transfer through mortar joints: a sharp-front analysis, Cement Concr. Res. 42 (2012) 1105–1112, https://doi.org/10.1016/j.cemconres.2012.05.004.
[17] H.J.P. Brocken, Moisture Transport in Brick Masonry: the Grey Area between Bricks, Ph.D. dissertation, Dept. Built Environment, Technische Universiteit Eindhoven, 1998.
[18] H. Derluyn, H. Janssen, J. Carmeliet, Influence of the nature of interfaces on the capillary transport in layered materials, Construct. Build. Mater. 25 (2011) 3685–3693, https://doi.org/10.1016/j.conbuildmat.2011.03.063.
[19] E. Vereecken, S. Roels, Hygric performance of a massive masonry wall: how do the mortar joints influence the moisture flux? Construct. Build. Mater. 41 (2013) 697–707, https://doi.org/10.1016/j.conbuildmat.2012.12.024.
[20] K. Calle, T. De Kock, V. Cnudde, N. Van den Bossche, Liquid moisture transport in combined ceramic brick and natural hydraulic lime mortar samples: does the hygric interface resistance dominate the moisture transport? J. Build. Phys. 43 (2019) 208–228, https://doi.org/10.1177/1744259119857762.
[21] X. Zhou, G. Desmarais, P. Vontobel, J. Carmeliet, D. Derome, Masonry brick–cement mortar interface resistance to water transport determined with neutron radiography and numerical modeling, J. Build. Phys. 44 (2020) 251–271, https://doi.org/10.1177/1744259120908967.
[22] V. Soulios, E. Jan de Place Hansen, R. Peuhkuri, Hygrothermal performance of hydrophobized and internally insulated masonry walls - simulating the impact of hydrophobization based on experimental results, Build. Environ. 187 (2021), 107410, https://doi.org/10.1016/j.buildenv.2020.107410.
[23] N.F. Jensen, S.P. Bjarløv, C. Rode, E.B. Møller, Hygrothermal assessment of four insulation systems for interior retrofitting of solid masonry walls through calibrated numerical simulations, Build. Environ. 180 (2020), 107031, https://doi.org/10.1016/j.buildenv.2020.107031.
[24] G. Castellazzi, S. de Miranda, G. Formica, L. Molari, F. Ubertini, Coupled hygro-mechanical multiscale analysis of masonry walls, Eng. Struct. 84 (2015) 266–278, https://doi.org/10.1016/j.engstruct.2014.11.034.
[25] X. Zhou, J. Carmeliet, D. Derome, Assessment of moisture risk of wooden beam embedded in internally insulated masonry walls with 2D and 3D models, Build. Environ. 193 (2021), 107460, https://doi.org/10.1016/j.buildenv.2020.107460.
[26] P.B. Lourenço, Computational Strategies for Masonry Structures, 1996.
[27] M. Petracca, L. Pelà, R. Rossi, S. Zaghi, G. Camata, E. Spacone, Micro-scale continuous and discrete numerical models for nonlinear analysis of masonry shear walls, Construct. Build. Mater. 149 (2017) 296–314, https://doi.org/10.1016/j.conbuildmat.2017.05.130.
[28] H. Ramézani, J. Jeong, Environmentally motivated modeling of hygro-thermally induced stresses in the layered limestone masonry structures: physical motivation and numerical modeling, Acta Mech. 220 (2011) 107–137, https://doi.org/10.1007/s00707-011-0463-5.
[29] J. Carmeliet, Influence of damage and moisture on the nonlinear hysteretic behavior of quasi-brittle materials, in: A.H. Kim, R.A. Guyer (Eds.), Nonlinear Elasticity and Hysteresis: Fluid-Solid Coupling in Porous Media, first ed., Wiley-VCH Verlag GmbH & Co. KGaA, Weinheim, Germany, 2015, pp. 81–104, https://doi.org/10.1002/9783527665068.ch4.
[30] H.M. Künzel, Simultaneous Heat and Moisture Transport in Building Components: One- and Two-Dimensional Calculation Using Simple Parameters, Ph.D. Dissertation, Dept. Building Physics, Fraunhofer Institute of Building Physics, 1995.
[31] J.L. Monteith, M.H. Shatleworth, Principles of Environmental Physics, fourth ed., Elsevier Ltd., London, 2013.
[32] RILEM Tc 25-Pem, Recommended tests to measure the deterioration of stone and to assess the effectiveness of treatment methods (Test No. I.1 Porosity accessible to water), Matériaux et Constructions 13 (1980) 176–179.
[33] BS EN ISO 15148:2002+A1:2016, Hygrothermal Performance of Building Materials and Products – Determination of Water Absorption Coefficient by Partial Immersion, 2016.
[34] ASTM E96/E96M-10, Standard Test Methods for Water Vapor Transmission of Materials, 2010, https://doi.org/10.1520/E0096.
[35] Bs En Iso 12572:2016, Hygrothermal Performance of Building Materials and Products – Determination of Water Vapour Transmission Properties – Cup Method, 2016.
[36] En 15803:2009, Conservation of Cultural Property - Test Methods - Determination of Water Vapour Permeability, 2009. δp.
[37] Bs En Iso 12571:2013, Hygrothermal Performance of Building Materials and Products – Determination of Hygroscopic Sorption Properties, 2013.
[38] En 16322:2013, Conservation of Cultural Property - Test Methods - Determination of Drying Properties, 2013.
[39] S. Brunauer, P.H. Emmett, E. Teller, Adsorption of gases in multimolecular layers, J. Am. Chem. Soc. 60 (1938) 309–319.
[40] Y. Mualem, A new model for predicting the hydraulic conductivity of unsaturated porous media, Water Resour. Res. 12 (1976) 593–622.
[41] M.Th van Genuchten, A closed form equation predicting the hydraulic conductivity of unsaturated soils, Soil Sci. Soc. Am. J. 44 (1980) 892–898.
[42] COMSOL, COMSOL Multiphysics ®, 2021. Version 6.0.

[43] G. Scheffler, Validation of Hygrothermal Material Modelling under Consideration of the Hysteresis of Moisture Storage, Ph.D. dissertation, Dept. Civil Engineering, Dresden University of Technology, 2008.
[44] M. Krus, Moisture Transport and Storage Coefficients of Porous Mineral Building Materials: Theoretical Principles and New Test Methods, Fraunhofer IRB Verlag, Stuttgart, 1996.
[45] Martin Krus, A. Holm, Simple methods to approximate the liquid transport coefficients describing the absorption and drying process, in: 5th Sympossium Building Physics in the Nordic Countries, Göteborg, 1999, pp. 241–248.
[46] J. Zhao, S. Feng, J. Grunewald, F. Meissner, J. Wang, Drying characteristics of two capillary porous building materials: calcium silicate and ceramic brick, Build. Environ. 216 (2022), 109006, https://doi.org/10.1016/j.buildenv.2022.109006.
[47] Z. Zhang, G. Scherer, Determination of water permeability for a moisture transport model with minimized batch effect, Construct. Build. Mater. 191 (2018) 193–205, https://doi.org/10.1016/j.conbuildmat.2018.09.194.
[48] A.M. D'Altri, S. de Miranda, G. Castellazzi, V. Sarhosis, A 3D detailed micro-model for the in-plane and out-of-plane numerical analysis of masonry panels, Comput. Struct. 206 (2018) 18–30, https://doi.org/10.1016/j.compstruc.2018.06.007.
[49] R.D. Prangnell, The water vapour resistivity of building materials: a literature survey, Matériaux et Constructions 4 (1971) 399–405.